energies

MDPI

Article

On Solar Radiation Prediction for the East–Central European Region

Michał Mierzwiak *, Krzysztof Kroszczyński and Andrzej Araszkiewicz

Faculty of Civil Engrineering and Geodesy, Military University of Technology, Gen. S. Kaliskiego 2, 00-908 Warsaw, Poland; krzysztof.kroszczynski@wat.edu.pl (K.K.); andrzej.araszkiewicz@wat.edu.pl (A.A.)
* Correspondence: michal.mierzwiak@wat.edu.pl

Abstract: The aim of this paper is to present the results of the Weather Research and Forecasting (WRF) model of solar radiation for moderate climatic zones. This analysis covered the area of northeastern Germany. Due to very unfavorable solar energy conditions in this region for at least 1/3 of the year, we decided to select the dates with the most representative conditions: passing warm fronts, cold fronts, and occluded fronts (two cases each). As the reference, two cloudless conditions during high-pressure situations were chosen. Two different shortwave radiation schemes—Rapid Radiative Transfer Model for general circulation model (RRTMG) and Dudhia—were tested. The obtained results were compared with in situ data measured at Deutscher Wetterdienst (DWD) stations and then with European Medium-Range Weather Forecast reanalysis (ERA5) data. The results showed that for high-pressure situations, the mean correlations with measured data were above 90%. The Dudhia scheme, in addition to the expected good results for the high-pressure situation, showed better results than RRTMG for the warm and cold fronts as well. The forecast using the RRTMG scheme gave the best results for the occluded front, which were also better than those of the ERA5 model.

Keywords: WRF; solar energy; weather prediction; solar radiation; meteorologic fronts

Citation: Mierzwiak, M.; Kroszczyński, K.; Araszkiewicz, A. On Solar Radiation Prediction for the East–Central European Region. *Energies* **2022**, *15*, 3153. https://doi.org/10.3390/en15093153

Academic Editor: John Boland

Received: 22 March 2022
Accepted: 23 April 2022
Published: 26 April 2022

1. Introduction

The European Union energy policy aims to systematically increase the share of electricity produced from renewable energy sources [1,2]. Photovoltaic panels, through the possibility of creating various sizes of installations and installation in various places, (e.g., on apartment buildings), are still gaining popularity. The use of modern production technologies and innovative technical solutions is driving installation costs lower and lower, resulting in even greater interest in this source of renewable energy. At the same time, the installations used to heat water in residential buildings or institutions are becoming more and more popular. This technology is based on the direct conversion of solar energy into thermal energy, which is used to heat up water for domestic use or as a support for heating systems [3–5]. One of the most important advantages of solar energy is that no pollutants are emitted in the process of converting it into electricity or heat [6]. Therefore, it is attracting increasing interest in various parts of the world—not only in those where solar conditions are most favorable (around tropical latitudes). Many studies have been related to methodologies for determining optimal locations for solar installations, using for this purpose, among others, Geographic Information System (GIS) tools or advanced analytical and statistical methods [7–9]. The choice of the best location for solar installations must take into account, first and foremost, the natural environmental conditions, geographical location, and infrastructural conditions. Most spatial analyses take into account the mean (climatic) solar conditions (determined on the basis of parameters derived from the Digital Elevation Model (DEM) and parameters related to the properties of solar radiation (solar angle, declination, etc.) [10–12].

Due to the growing popularity of photovoltaic installations and the increasing share of electricity they produce, forecasting future and potential energy yields is increasingly

important. This is especially important for power utilities [13]. To find this parameter, it is necessary to have information about the amount of radiation reaching the Earth's surface directly from the Sun. The forecast of this element allows for an estimation of the amount of energy that can be obtained from photovoltaic installations in a given region. However, solar conditions considered during the selection of location often differ from the real values, which depend strongly on the actual meteorological conditions. Therefore, there is a need for solar forecasts using other tools such as numerical weather prediction models. Nowadays, NWP data are widely used to predict weather conditions for short-, medium- and long-term forecasts. There are many classifications of models, which can be divided, among other things, according to the area for which forecasts are generated (models: global, mesoscale, regional, etc.). The models that cover a specific region are characterized by better effects, and thanks to an appropriate parameterization of the model, it is possible to obtain optimal simulation results. Among the numerical weather prediction models, (e.g., Global Forecast System (GFS) [14], Unified Model (UM) [15], European Medium-range Weather Forecast (ECMWF) [16], Icosahedral Nonhydrostatic Model (ICON) [17]), the Weather Research and Forecasting model (WRF) [18] is very popular. It is an example of a nonhydrostatic mesoscale weather forecast model. It is used in many countries (over 160), both by institutions involved in statutory weather forecasting (for operational purposes) and for research/scientific purposes [19]. Its great advantage is that it is available free of charge.

Numerical weather prediction models are used for various purposes, not only to predict weather conditions. These models are valuable tools for forecasting various phenomena and processes occurring in the natural environment. They are used, among other things, to estimate the risk of forest fires [20], forecast the occurrence of fog (in the context of solar energy harvesting) [21], model the amount of energy harvested from wind turbines [22], generate short-term forecasts of wind energy [23], etc. With growing interest in forecasts of solar conditions, a dedicated version of the WRF model—WRF-Solar—has been released. Originally, it was based on WRF-3.6 and was an independent product; later (since WRF-4.2), it became an integral part of the WRF model, the functionality of which can be used by applying an appropriate configuration of parameters [24–27].

In the literature, most interest has been given to regions with very favorable solar conditions—areas around the tropics [28,29]. Many analyses have also been carried out for European countries at lower latitudes such as: Greece, Spain, Romania, and Turkey [30–33]. There is much less work related to regions at higher latitudes, such as Central and Northern Europe [34,35]. According to the currently valid version of the Köppen–Geiger classification of world climates (1980–2016), Central Europe is located in the temperate latitude climate zone of the humid continental variety (Dfb), without a dry season with a warm summer season [36]. The map showing the future distribution of climate zones (for 2071–2100) clearly shows that the analyzed region will be characterized by different conditions—climate zones Cfa/Cfb (humid subtropical/maritime climate of middle and high latitudes (25° to 70° N)) [36]. The above indicates that the current conditions are not the most favorable ones, (e.g., in terms of the amount of cloud cover, dynamic changes in atmospheric conditions, etc.), while in the future, they will be much better in the context of obtaining energy, e.g., from solar radiation. The intensified movement of extratropical cyclones of middle latitudes observed in recent years, especially in the cold season [37], contributes to making it even more difficult to predict atmospheric conditions. Although studies conducted on future changes of cyclones of middle latitudes indicate that over time their number and intensity will decrease and weaken [38,39], for the time being, they pose a serious challenge to meteorologists and governments of countries that have to deal with their severe (socio-economic) impacts [38,40,41].

The purpose of this study was to evaluate the feasibility of predicting solar radiation in temperate areas with high cloud cover. The analysis was carried out for the area of northeastern Germany. One of the most difficult meteorological elements to forecast is cloud cover, which is at the same time a very important factor determining solar radiation

delivery to the Earth's surface (especially direct radiation). Ongoing research on the automation of the atmospheric fronts detection process, using for this purpose, among other things, neural networks, has also been characterized by varied results [42]. The choice of the area was intentional—to verify the effectiveness of forecasts in a region characterized by high dynamics of atmospheric phenomena. Northeastern Germany is characterized by a significant number of atmospheric fronts moving from the west of the continent toward the east. The number of days with atmospheric fronts is more than 130 per year, so for almost one-third of the year, there are conditions of high cloudiness. Studies on longer time series show that for almost 40% of days in a year, atmospheric fronts move over the region [42,43]. Therefore, it is important to accurately predict the amount of solar radiation reaching the surface of the Earth during such unfavorable weather conditions.

2. Materials and Methods

The study region is situated between 52° and 55° latitude and between 11.5° and 14° east longitude, which means that the sunlight conditions there are much less favorable than, e.g., in southern Europe, the Middle East, or North Africa. On the other hand, the region is characterized by favorable location conditions for photovoltaic installations due to the topography (especially near the Seehausen station). In the analyzed area, during the summer months, with good weather conditions (slight cloudiness), one can count on significant amounts of energy generated from solar radiation (both thermal and electrical). However, in the autumn and winter seasons, due to the shorter day length, the sun's lower elevation, and the numerous atmospheric fronts moving over the region, the amount of radiation reaching the surface of the Earth is significantly lower.

Data from eight days were analyzed, representing four different synoptic situations (two cases each: cold front, warm front, occluded front, and high-pressure situation). The choice of specific dates was preceded by an analysis of synoptic maps (see Section 2.1). The dates were selected in accordance with the dominant atmospheric conditions on the analyzed day (Table 1).

Table 1. Summary of analyzed dates.

Date	Synoptic Situation	Cloud Cover	Clouds	Dynamic Change
14032020	high pressure situation	cloudless conditions	-	low
14092020				
11052020	cold front	overcast/broken conditions	convective clouds	medium
28062020				
24022020	warm front	overcast conditions	high-, middle-, and low-level clouds	high
22052020				
26082020	occluded front	variable cloudiness	convective clouds	medium/high
06102020				

For the analyzed region, simulations were performed under typical atmospheric conditions, such as high cloud cover caused by moving atmospheric fronts. A dedicated WRF configuration was used to obtain solar parameters—WRF Solar (further described in Section 2.2). The forecast was carried out in three variants differing with respect to wave radiation scheme. The following were used here: Rapid Radiative Transfer Model for general circulation model (RRTMG), Fast All-sky Radiation Model for Solar application (RRTMG-FARMS), and Dudhia (see Section 2.2 for details). From these, the direct radiation data referred to as SWDDIR (shortwave surface downward direct irradiance) and SWDDIR2 (shortwave surface downward direct irradiance from FARMS), were extracted. These values were compared with ERA5 reanalyses (a high-spatial-resolution dataset created using 4D-Var assimilated data and a predictive model (total sky direct solar radiation at the surface

(fdir)—the amount of solar radiation reaching the surface (flat horizontal plane) of the Earth) [44,45]). All of these employed data measured at Deutscher Wetterdienst (DWD) stations located in Arkona (WMO code: 10091; station_id: 00183), Rostock-Warnemünde (WMO code: 10170; station_id: 04271) and Seehausen (WMO code: 10261; station_id: 04642) [46]. For a more complete representation of the differences obtained between the model data and the measured data, the following statistical methods were used, the combination of which allows a better assessment of the reliability of the data: root mean square error (RMSE), mean absolute error (MAE), mean bias error (MBE).

$$\mathrm{RMSE} = \sqrt{\frac{\sum_{i=1}^{N}(\text{model data } (\mathrm{WRF})_i - \text{measured data } (\mathrm{DWD})_i)^2}{N}} \quad (1)$$

$$\mathrm{MAE} = \frac{1}{N}\sum_{i=1}^{N}|\text{model data } (\mathrm{WRF})_i - \text{measured data } (\mathrm{DWD})_i| \quad (2)$$

$$\mathrm{MBE} = \frac{1}{N}\sum_{i=1}^{N}(\text{model data } (\mathrm{WRF})_i - \text{measured data } (\mathrm{DWD})_i) \quad (3)$$

These statistics are among the most commonly used in evaluating weather forecasts on the basis of numerical models [3,35,47]. RMSE is a common statistical method used in, e.g., meteorology, to measure the effectiveness of models. Its trademark is to give a higher weight to errors connected with larger absolute values than to those connected with smaller ones. MAE measures mean error and the distribution of their magnitudes. MBE indicates the average model bias, especially under- or over-prediction of the WRF forecast, in this case [13,48,49]. Additionally, statistics were normalized by mean measured value and expressed as normalized root mean square error (nRMSE) and normalized MBE (nMBE). In order to validate the model data (WRF simulations), temperature values at 2 m above (the) sea level (a.s.l.) were compared with data measured in situ at meteorological stations.

The three stations with actinometric data (Arkona, Rostock-Warnemünde, Seehausen) are located at different sites: Arkona (54.6792 N, 13.4343 E, 42 m a.s.l.) is the northernmost and is located on the island of Rügen, on the rocky Cape Arkona; the station Rostock-Warnemünde (54.1803 N, 12.0808 E, 4 m a.s.l.) is located on the Bay of Mecklenburg; the third station, Seehausen (52.8911 N, 11.7297 E, 21 m a.s.l.), is located inland. Arkona and Rostock-Warnemünde are located in the southwest Baltic coastal area and the Mecklenburg coastal area, which are characterized by low moraine plains with moraine hills above 100 m above sea level [50].

2.1. Synoptic Situations

This section describes the synoptic situations selected for the study. The analysis was based on synoptic maps prepared by the Polish Institute of Meteorology and Water Management–National Research Institute (IMGW-PIB) [51].

On 14 March 2020 (Figure 1a), a stationary high-pressure system with a center over the study area (1026 hPa) shaped the weather in the region. There were no inversions at this time, resulting in no cloud cover (sub-inversion). On 14 September 2020 (Figure 1b), the analyzed area was located in the western part of an extensive stationary high-pressure system with its center over the western outer Carpathians (1029 hPa); cloudiness and other phenomena did not occur.

The next situation (24 February 2020) concerned the transition of a warm front, with its characteristic extensive zone of cloudiness, mainly shaped by stratiform clouds (Figure 2a). On 24 February 2020, the weather in the analyzed region was initially influenced by a ridge associated with a high-pressure system centered over the Iberian Peninsula (1033 hPa), and then under the influence of a low-pressure system with a trough centered over Scotland (993 hPa) and associated with an active warm front. On that day, the sequence of clouds was characteristic of a warm front, created first by high clouds, then by middle clouds, and finally by low clouds. The frontal system experienced continuous rainfall, changing to a

drizzle later on. On 22 May 2020 (Figure 2b), the weather in the region was shaped into a trough associated with a deep low-pressure system with a center located northwest of Scotland (972 hPa) and an associated warm front moving towards the east. That day, there was total cloud cover, formed by clouds, first high, and then medium, passing to stratiform low clouds. The overcast was accompanied by continuous rain, which turned into drizzle after the front passed through.

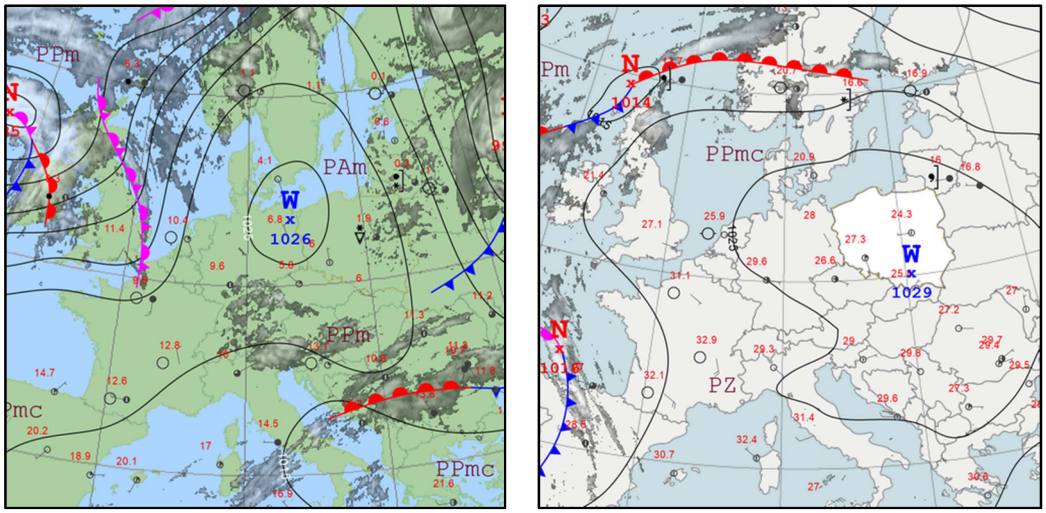

(**a**) (**b**)

Figure 1. Synoptic maps from IMGW-PIB for the situations of: (**a**) 14 March 2020; and (**b**) 14 September 2020 (high-pressure situation).

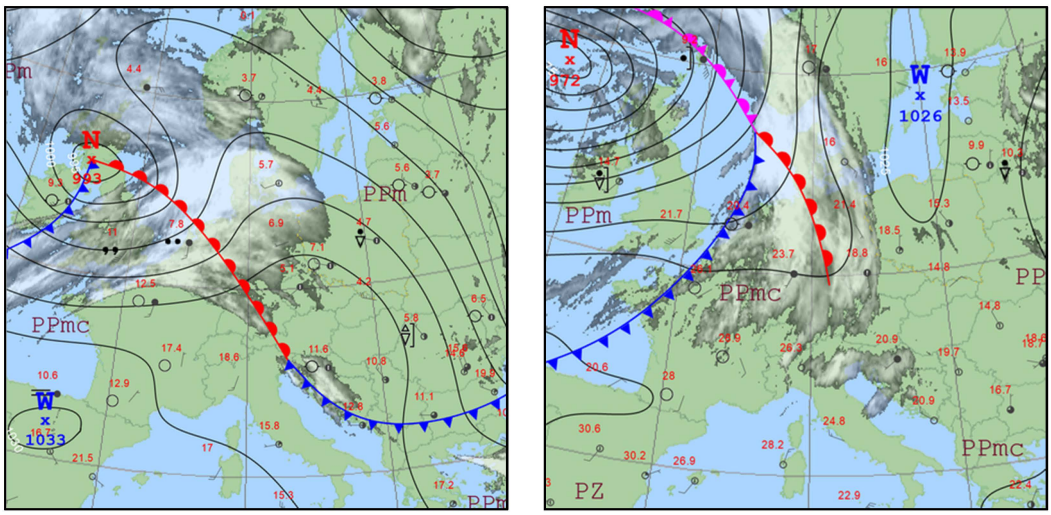

(**a**) (**b**)

Figure 2. Synoptic maps from IMGW-PIB for the situations of: (**a**) 24 February 2020; and (**b**) 22 May 2020 (warm front).

On 11 May 2020 (Figure 3a), the weather in the northeastern part of Germany developed behind an undulating cold front associated with a low centered over the northern part of the Scandinavian Peninsula. The weather was cloudy with convective clouds and occasional showers. Cloudy to variable. On 28 June 2020 (Figure 3b), the weather in the region was influenced by a shallow trough associated with the center of the filling low with its center over the northern part of Scotland (986 hPa) and an associated cold front. There was total cloud cover changing to variable (middle-level clouds and Cumulonimbus). There was some rainfall.

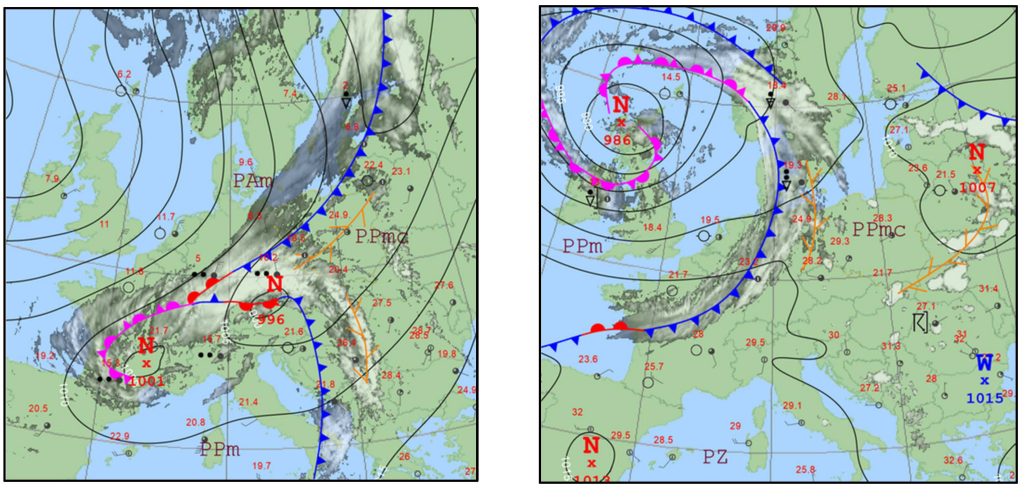

(**a**) (**b**)

Figure 3. Synoptic maps from IMGW-PIB for the situations of: (**a**) 11 May 2020; and (**b**) 28 June 2020 (cold front).

On 26 August 2020 (Figure 4a), the analyzed region was under the influence of a trough associated with the filling low with its center over the Jutland Peninsula (994 hPa) and an occlusion front with the character of a cold front, in unstable air mass. There was variable cloudiness accompanied by brief rainfall and thunderstorms. On 6 October 2020 (Figure 4b), the weather over the northeastern part of Germany was shaped under the influence of a shallow trough associated with a slightly active, filling low-pressure system with its center over the North Sea (992 hPa) and an associated occlusion front. Variable cloudiness was present.

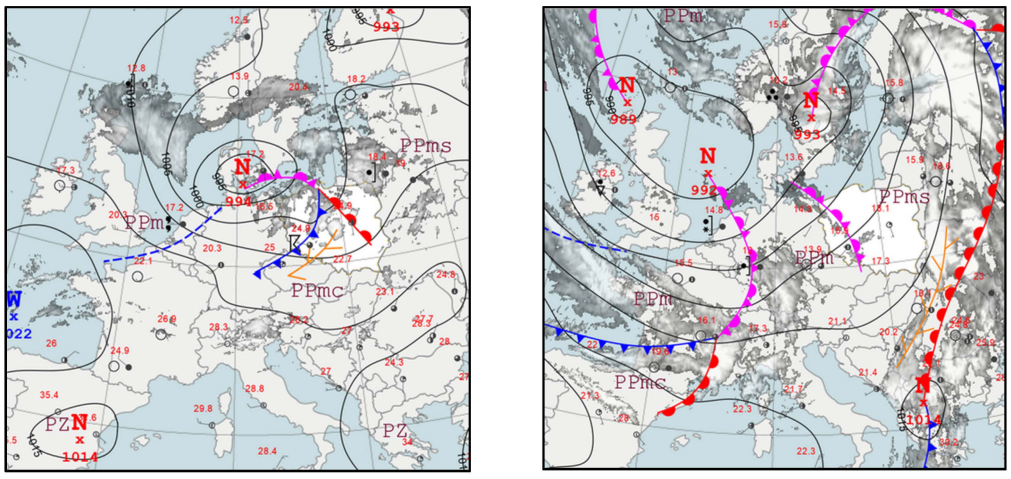

(**a**) (**b**)

Figure 4. Synoptic maps from IMGW-PIB for the situations of: (**a**) 26 August 2020; and (**b**) 6 October 2020 (occluded front).

2.2. WRF Schema

WRF model ver. 4.2.1 was run for GFS input data [52] with a spatial resolution of 0.25° and a temporal resolution of 3 h. Two domains (ratio 3), with 3000 and 1000 m resolution (d01 and d02 in Figure 5), were used for Lambert conformal mapping. The second domain covered the analyzed area. WRF simulations were started (for each of the eight situations) at 00:00 and ran for 24 h with a starting interval of 1 h.

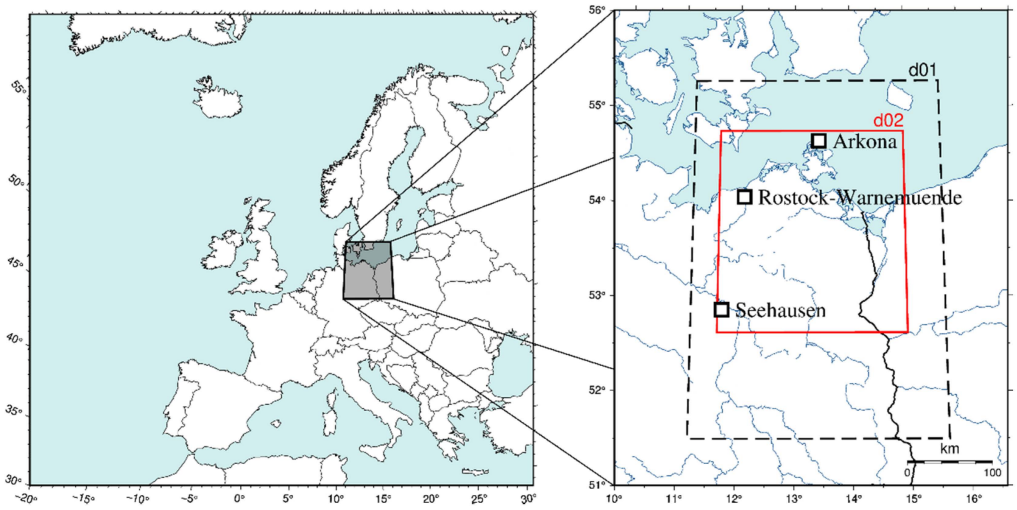

Figure 5. Overview map of the study area with marked DWD stations and the domains used in WRF.

The following set of parameters was used in the model: Thompson microphysics scheme, the boundary layer represented by the Mellor-Yamada Nakanishi and Niino schemes, the shortwave radiation process parametrized by the Rapid Radiative Transfer Model for general circulation models (RRTMG) scheme (model configuration consistent with the WRF Solar [24,27]) and by the Dudhia scheme, surface layer—revised MM5 Scheme, land surface—Unified Noah Land Surface Model, and shallow cumulus represented by the Deng scheme [18,27,53–55] (Table 2). Additionally, the other model option—the FARMS scheme—was tested, which uses the current physical state of the atmosphere, including hydrometeors, to determine the radiation reaching the Earth's surface [56]. The main difference between the Dudhia scheme and RRTMG is the complex nature of the latter. The simulation takes into account the aerosols present in the atmosphere, which affect, among other things, the amount of cloudiness of the solar radiation supply [57]. Finally, the resulting data include WRF model simulations using two shortwave radiation schemes, RRTMG and Dudhia; for the former, it was possible to acquire the determined parallel direct radiation using the FARMS scheme. In this paper, they are tagged as RRTMG, RRTMG(F), and Dudhia, respectively.

Table 2. WRF physics option configuration.

Model	Chosen Configuration
Horizontal resolution	d01: 3000 (m)
	d02: 1000 (m)
Vertical resolution	45 levels
Microphysics	Thompson Scheme
Planetary boundary layer	Mellor-Yamada Nakanishi Niino (MYNN)
Longwave radiation scheme	RRTMG
Shortwave radiation schemes	Dudhia/RRTMG
Land surface options	Unified Noah Land Surface Model
Shallow cumulus option	Deng Scheme
Surface layer options	Revised MM5 Scheme

3. Results

In order to validate the WRF model simulation data, a summary comparison was made between air temperature values (2 m a.s.l.) and data obtained from meteorological stations

(surface synoptic observations—SYNOP messages [58]): Arkona, Rostock-Warnemünde and Seehausen. The mean value of the absolute difference in temperature (at 2 m a.s.l.), obtained from the measurement data and the RRTMG model for the Arkona station was 0.93 °C, for Rostock it was 1.21 °C, while for Seehausen it was 1.11 °C. For Dudhia, for Arkona, the difference was 1.14 °C, for Rostock-Warnemünde station, it was 1.64 °C, and for Seehausen it was 1.15 °C. The correlation of forecast temperature with measured temperature for each scenario was above 97%. The above confirms the high fit of the simulated (forecast) data to the readings from the meteorological stations. All stations were characterized by low RMSE and nRMSE values for both WRF simulations (RRTMG and Dudhia). The values were, respectively: Arkona: 1.93 (16.2%) and 1.92 (16.1%); Rostock-Warnemünde: 1.54 (12.1%) and 1.61 (12.6%); Seehausen: 1.49 (12.0%) and 1.54 (12.4%). Figure 6 presents the daily distribution of mean differences in temperature values for the three stations and scatter plots for the compiled temperature values: forecasted and measured at DWD stations.

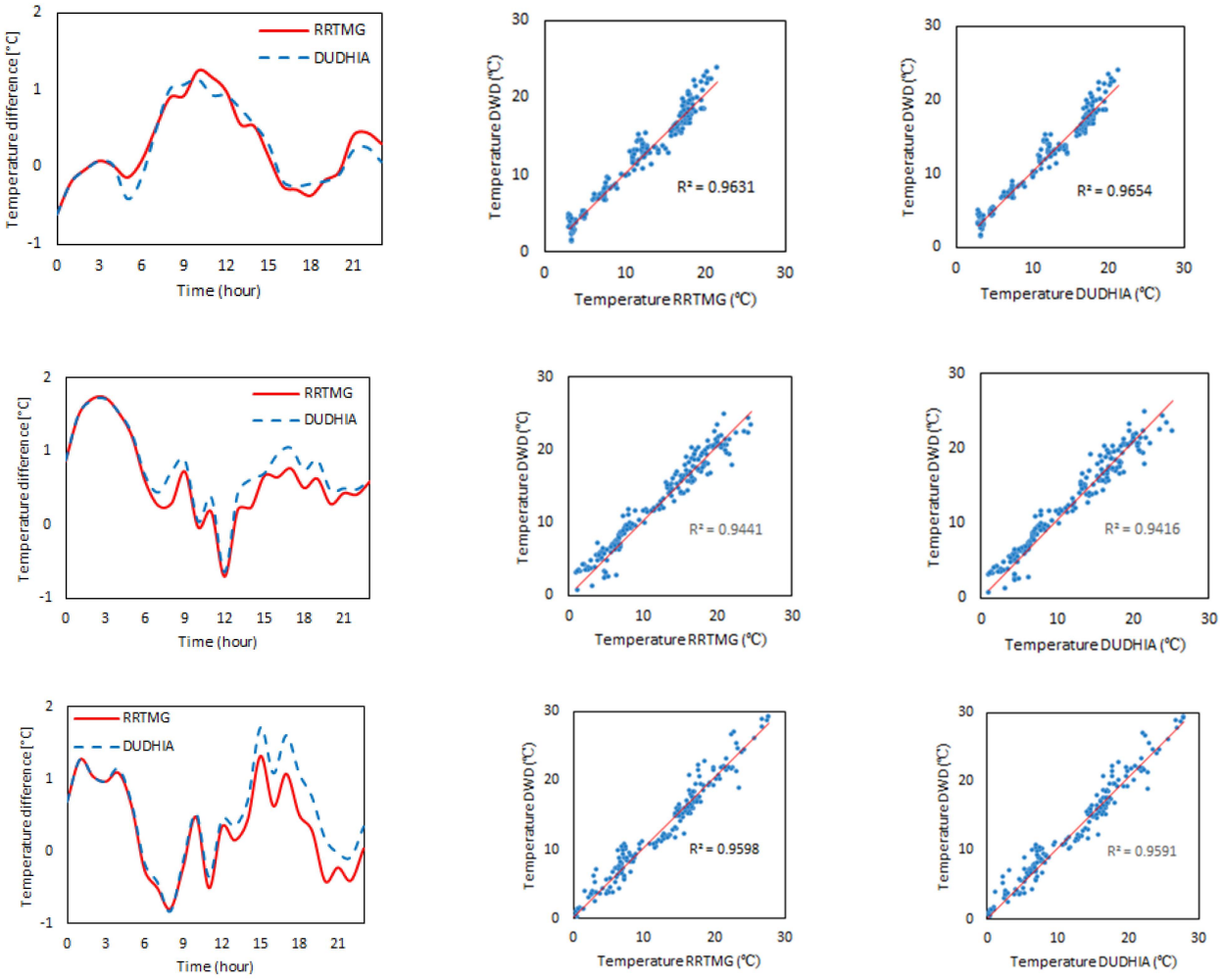

Figure 6. Graphs showing the average air temperature differences (left) and their scatter [°C], from top: Arkona, Rostock-Warnemünde, and Seehausen.

The following sections present daily distributions of the direct solar radiation reaching the Earth's surface at the analyzed stations for each of the eight dates. Data from WRF model simulations (RRTMG, RRTMG(F), and Dudhia), ERA5, and the results of direct measurements carried out at the stations (DWD) are summarized. The results are grouped for each synoptic situation. The resulting values of solar radiation were converted to the same unit [W·m^{-2}].

3.1. High-Pressure System

For the high-pressure situation (14 March 2020 and 14 September 2020) (no cloud cover), the WRF model simulation results were very close to the values recorded by the ground stations. Maps showing direct radiation for 14 March 2020 at 12:00, obtained from RRTMG and Dudhia simulations, differed in the vast majority of the area by a constant value (Figure 7). The Dudhia configuration was characterized by higher values, which were much closer to those obtained from direct measurements (this is also visible on graphs presenting the daily distributions of the analyzed parameters). Such systematic differences were obtained for most epochs.

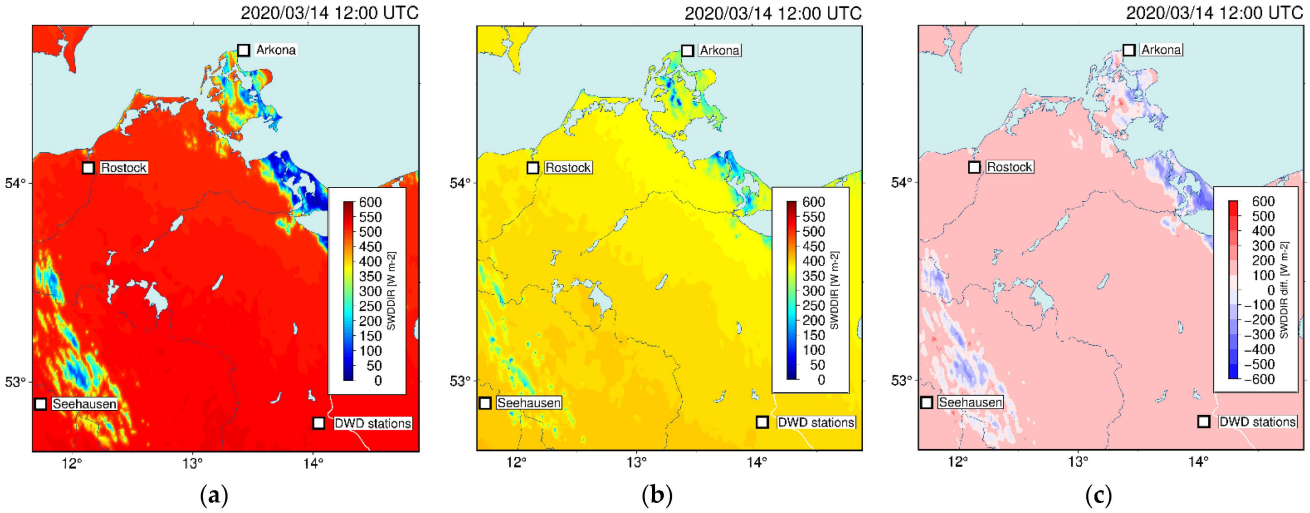

Figure 7. Shortwave surface downward direct irradiance (SWDDIR) forecast for 14 March 2020 at 12:00 for: (**a**) Dudhia; (**b**) RRTMG; and (**c**) their differences.

The plots above (Figure 8) show the diurnal course of direct radiation values derived from measured data (DWD), the WRF model (using RRTMG and Dudhia scheme), and ERA5 reanalyses (ECMWF). The following graphs show a similar shape to the curves. The values obtained from RRTMG are characterized by lower values than the measured data, while the application of the Dudhia scheme made it possible to achieve direct radiation values similar to those measured in situ. The mean value of the absolute difference for Dudhia is 19.51 $W \cdot m^{-2}$; for ERA5 is 30.10 $W \cdot m^{-2}$, and for RRTMG is 54.62 $W \cdot m^{-2}$.

Pearson's correlation coefficient was determined for the above situations to determine the relationship between predicted and measured data (Table 3). They indicate a very strong correlation between WRF model data (especially for the Dudhia shortwave radiation scheme) and DWD. The mismatched RRTMG(F) forecast for the Arkona station on 14 March 2020 resulted in a decrease in the mean correlation coefficient to 54%. On the second analyzed date (14 September 2020), the forecast was fine and showed the absence of cloud cover.

Table 3. Summary of correlation coefficients for high situations.

Station	RRTMG	RRTMG(F)	Dudhia	ERA5
Arkona	0.91	0.54	0.99	0.99
Rostock-Warnemünde	0.99	0.99	0.97	0.98
Seehausen	0.99	0.99	0.99	0.95

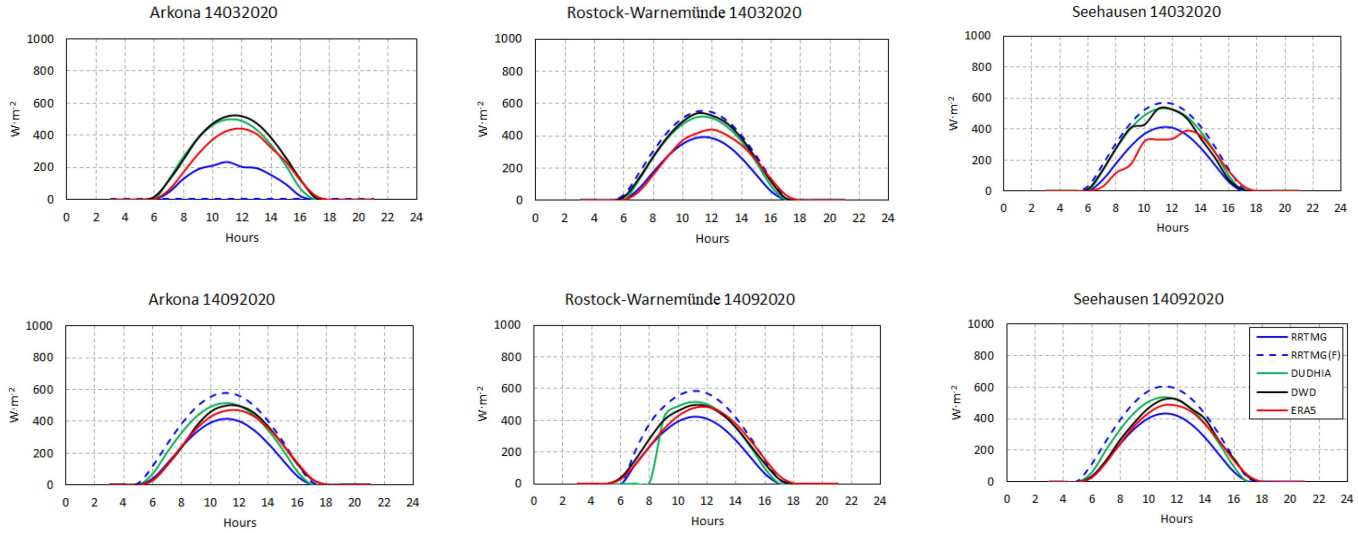

Figure 8. Diurnal distribution of the direct radiation values for the high situations.

3.2. Warm Front

The Dudhia simulation for 1 p.m. on 22 May 2020 (Figure 9) showed a smaller area of the analyzed region that was reached by direct radiation. RRTMG configuration predicted the radiation delivery slightly differently (smaller parameter values—higher cloudiness), especially in the eastern and southeastern parts of the region. The largest differences between the models occurred at the cloud boundary. In addition, on 22 May Dudhia indicated a thinner cloud layer in a band from the coast toward the southeast, through which the radiation passed. In the case of RRTMG, this area remained shaded.

Analysis of the daily distribution of radiation at the analyzed stations (Figure 10) shows its more complex course. This is due to the increase in the amount of cloudiness associated with the passage of the front. The following figure shows clearly larger values represented by the WRF model (both for RRTMG and Dudhia scheme), although for the situation on 22 May 2020 at Arkona and Rostock-Warnemünde, the correlation with DWD data was very strong.

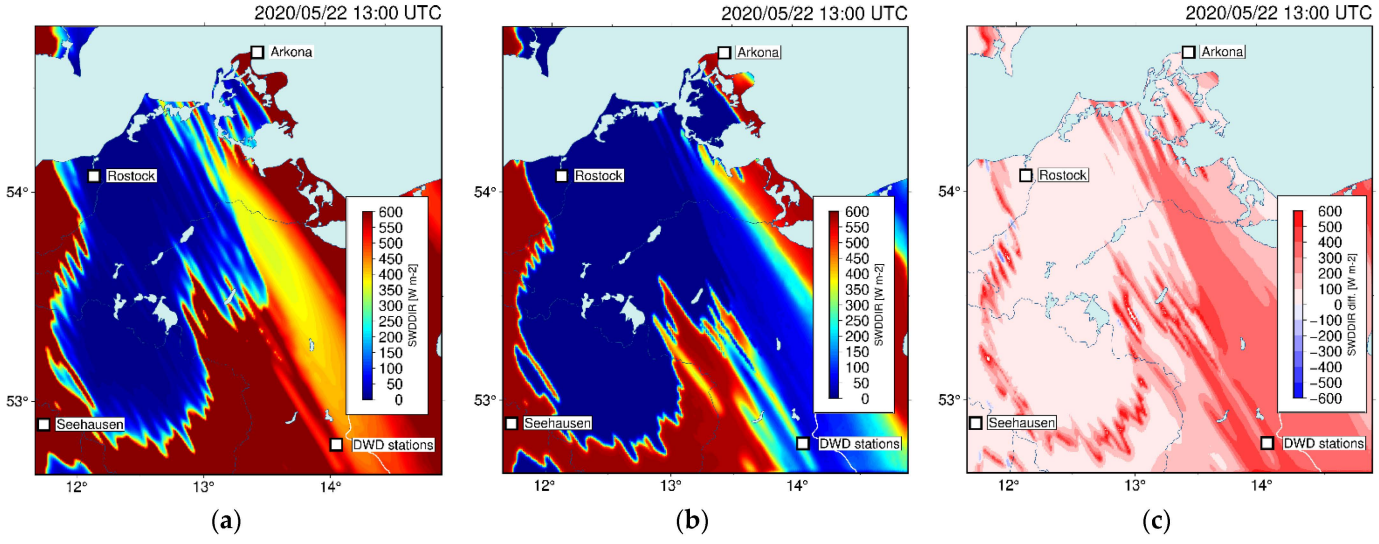

Figure 9. Shortwave surface downward direct irradiance (**SWDDIR**) forecast for 22 May 2020 at 13:00 for: (**a**) WRF-Dudhia; (**b**) WRF-RRTMG; and (**c**) their differences.

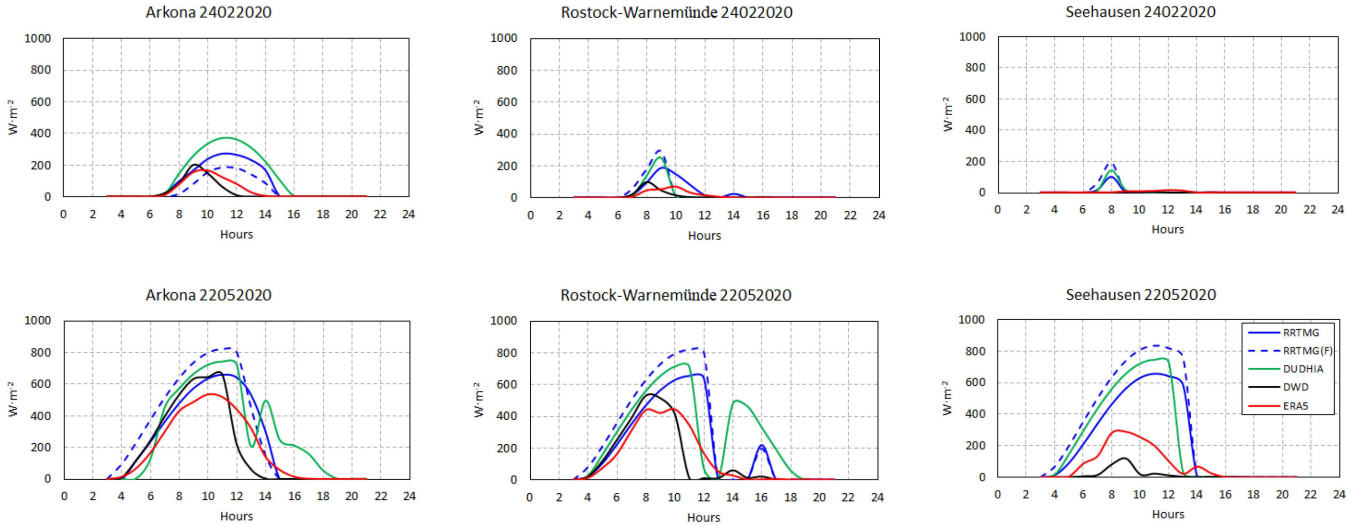

Figure 10. Diurnal distribution of the direct radiation values for the warm fronts.

The WRF models, especially on 22 May 2020 for Arkona and Rostock, with some delay, modeled the appearance of cloudiness related to the moving atmospheric front. Additionally, for Rostock, the interruption of direct radiation was supposed to last about 1 h; in fact, the cloudiness persisted until the end of the day. For the Seehausen station, both WRF simulations and reanalysis data (ERA5) were significantly overestimated (especially WRF). At Arkona on 24 February 2020, the WRF model in both variants did not forecast a warm front; in the case of Rostock station, the forecasts of direct radiation delivery were overestimated with respect to the value and time of its arrival at the Earth's surface. At Seehausen on 24 February 2020, direct solar radiation did not break through the cloud layer. Table 4 presents the values of correlation coefficients between forecast data, ERA5, and measured data.

The forecast distribution of solar radiation totals during the movement of the warm front showed to be close to the values of the ground data. Among the forecast models, the RRTMG(F) (mean: 0.743) model turned out to be the best, giving about 14% worse results than ERA5 (mean: 0.883). There is a noticeable decreasing tendency of correlation coefficient values (which corresponds to incorrect modeling of weather conditions—passage of fronts) with increasing distance from the Baltic Sea.

Table 4. Summary of correlation coefficients for warm fronts.

Station	RRTMG	RRTMG(F)	Dudhia	ERA5
Arkona	0.82	0.90	0.79	0.92
Rostock-Warnemünde	0.67	0.71	0.73	0.88
Seehausen	0.62	0.62	0.67	0.84

3.3. Cold Front

The passage of a cold front was analyzed for two dates: 11 May 2020 and 28 June 2020. As in the case of the passage of a warm front, the complex pattern of values of direct radiation reaching the Earth's surface was also characteristic, and the delivery of which was strongly dependent on the amount of cloud cover associated with the occurrence of cold fronts. The example maps (Figure 11) show the differences in direct radiation values at 10:00 a.m. on 28 June 2020 across the analysis area. Numerous (especially in the case of Dudhia) small areas receiving direct radiation can be seen (in contrast to the RRTMG forecast). In contrast, the areas receiving high radiation values generally overlap (on both maps).

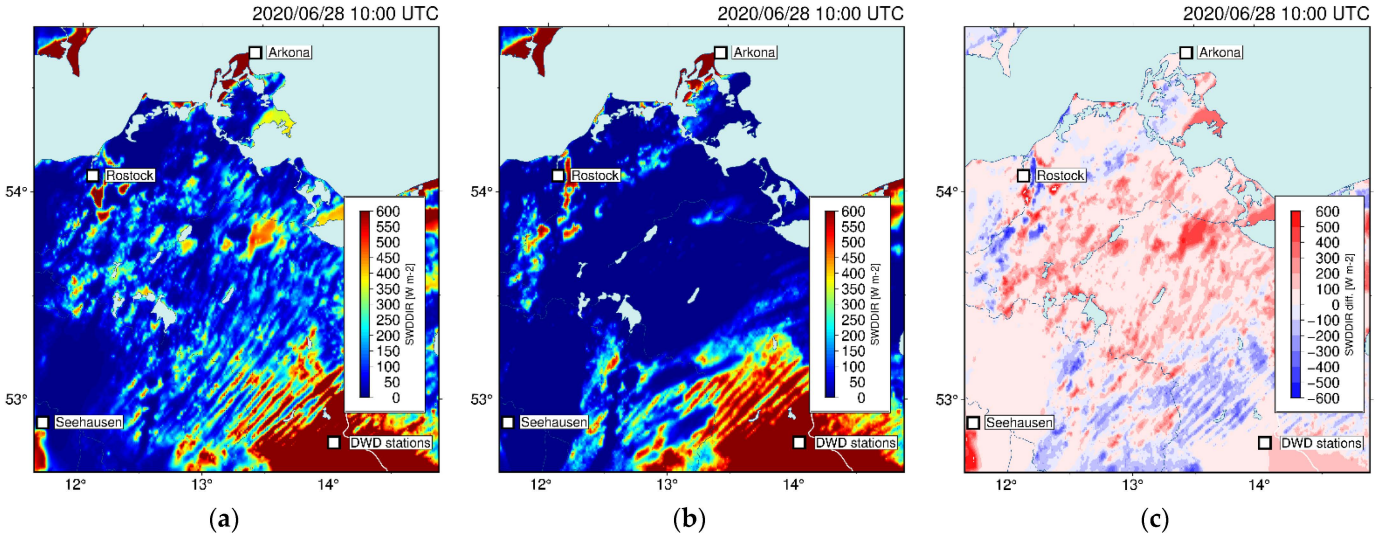

Figure 11. Shortwave surface downward direct irradiance (**SWDDIR**) forecast for 28 June 2020 at 10:00 for: (**a**) WRF-DUDIA; (**b**) WRF-RRTMG; and (**c**) their differences.

On 11 May, one can see the "co-shaping" of the curve created by the WRF model results with respect to the curve representing data from the ground measurements (Figure 12). In the case of Arkona, on 11 May 2020, the forecast predicted an earlier/quicker movement of the front—in fact, the cloud cover receded almost 4 h later (around 13:00). In Rostock, the reverse occurred—the sky cleared earlier by about 2 h. For the Seehausen site, Dudhia was clearly forecast wrongly—the cloud cover connected with the cold front actually lasted until 2 p.m.

On 28 June 2020, the distribution of radiation during the day differed considerably between the model data and measured values, which is evident, especially in the case of Rostock, where the highest values were achieved by the model when the measured values reached their minimum, after 12:00 p.m., or in Seehausen in the morning hours (until 9:00 a.m.). In the case of Arkona, the model predicted direct radiation values of about 400 $W \cdot m^{-2}$ around 16:00, although, in reality, cloud cover effectively blocked its delivery for the rest of the day. In this case (28 June 2020), for all stations, better results were obtained for Dudhia, where the values were much closer to the real conditions than for the RRTMG and RRTMG(F) models.

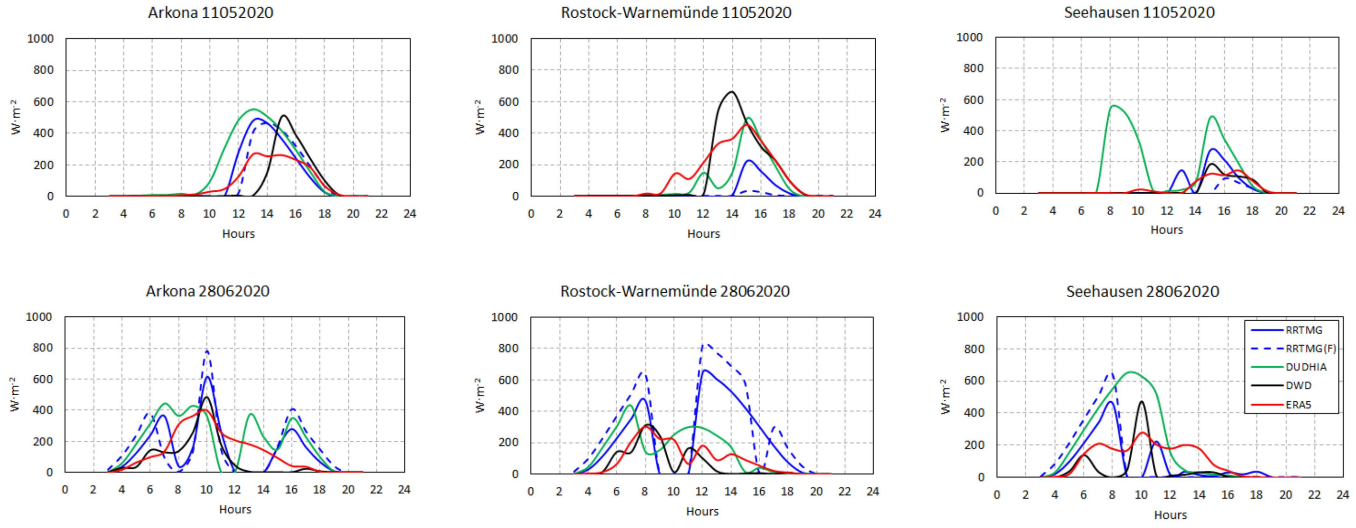

Figure 12. Diurnal distribution of the direct radiation values for the cold fronts.

The correlation coefficients for the situation associated with the passage of a cold front (Table 5) were significantly lower than those for a warm front or a high-pressure system. The mean results indicate the advantage of the Dudhia model. However, the best correlation was obtained for the RRTMG and RRTMG(F) models at Arkona station.

Table 5. Summary of correlation coefficients for cold fronts.

Station	RRTMG	RRTMG(F)	Dudhia	ERA5
Arkona	0.64	0.68	0.45	0.75
Rostock-Warnemünde	0.07	−0.02	0.49	0.84
Seehausen	0.17	0.62	0.49	0.60

3.4. Occluded Front

The last two situations (26 August 2020 and 6 October 2020) are related to the occurrence of an occluded front characterized by a complex cloud structure. The first phase is similar to that of a warm front and then similar to that of a cold front (Cumulonimbus (Cb) clouds). Maps presenting the direct radiation forecast for 6 October, at 9:00 a.m. (Figure 13), show only the systematic difference between values of the parameters (Dudhia is characterized by higher values than RRTMG). Spatial distribution and the size of areas not receiving direct radiation are very close to each other (almost identical).

The situation with occluded fronts (Figure 14) shows a significant difference between the two situations, with some of the lowest direct radiation values recorded on 26 August 2020 (DWD data). For the Seehausen site, both WRF models and ERA5 reanalyses were characterized by clearly overestimated values. The total direct radiation at the DWD station on that day was only 30.6 $W \cdot m^{-2}$.

On 6 October 2020, both measured and observed values were similar in Arkona. At the other sites, the maximum values occurred at different times of the day—at Seehausen, the highest predicted values occurred in the morning (8:00–10:00), while the actual maximum occurred in the afternoon (12:00–14:00). The model incorrectly predicted cloudiness limiting the access of direct radiation due to a moving atmospheric front (occluded). Interestingly, for this day, the ERA5 data also overestimated the values, even more than the WRF forecasts.

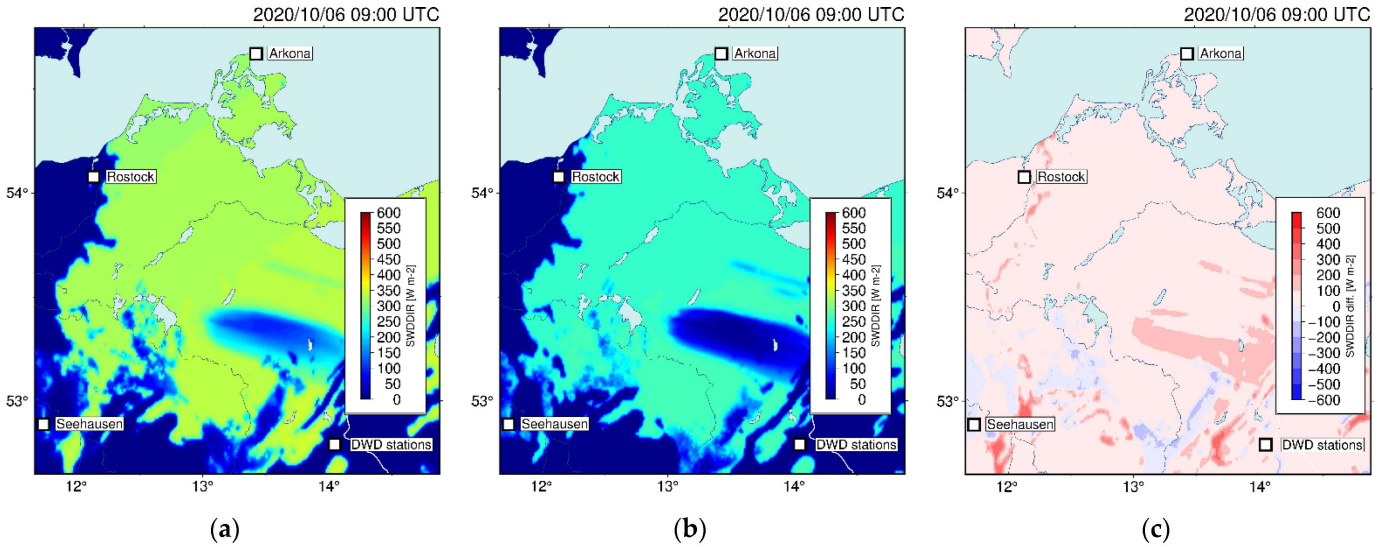

Figure 13. Shortwave surface downward direct irradiance (**SWDDIR**) forecast for 6 October 2020 at 09:00 for: (**a**) WRF-DUDIA; (**b**) WRF-RRTMG; and (**c**) their differences.

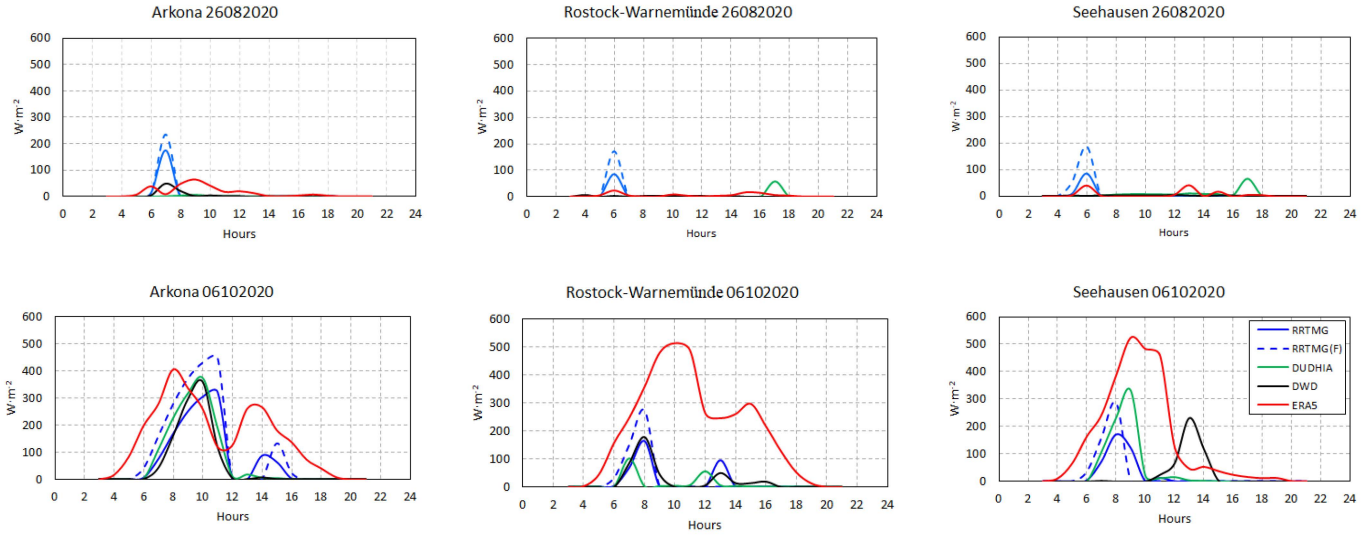

Figure 14. Diurnal distribution of the direct radiation values for the occulted fronts.

Pearson's correlation coefficients (Table 6) reached their lowest values at the Seehausen location. The highest similarity was found for the data at the Arkona station. As in the case of warm and cold fronts, the cloudiness associated with their presence caused such large discrepancies between forecast and observed data. In the case of Arkona, the correlation was quite strong, Rostock-Warnemünde showed a moderate correlation, while Seehausen showed no correlation at all between the data ($r < 0.2$).

Table 6. Summary of correlation coefficients for occluded fronts.

Station	RRTMG	RRTMG(F)	Dudhia	ERA5
Arkona	0.86	0.87	0.98	0.61
Rostock-Warnemünde	0.85	0.81	0.28	0.46
Seehausen	−0.09	0.06	−0.7	0.01

4. Discussion

A comparison of the errors (RMSE, nRMSE, MAE, MBE, nMBE) for the WRF and ERA5 model values shows that the ECMWF data were more similar to the observed data (Table 7), as expected. In both cases, the lowest values were obtained for the high-pressure situation, while the WRF model data proved to be more accurate for the occluded front (Tables 8–10), relative to the ERA5 reanalyses. A common feature of the model data was the underestimation of direct radiation in the high-pressure situation (nMBE: RRTMG: −29.14%; RRTMG(F): −1.72%; Dudhia: −1.95%; ERA5: −12.72%). In other cases, both WRF and ERA5 data were overestimated relative to observations (DWD), nMBE from 19.01% to 112.17%, 19.20% to 154.04%, and 20.19% to 124.37%, respectively. The WRF forecast results show that the Arkona station was characterized by having the smallest errors, while in the case of ERA5 reanalyses, the smallest errors were found for the Rostock-Warnemünde station.

Table 11 shows the correlation coefficients for specific synoptic situation types. For the high-pressure situations (14 March 2020 and 14 September 2020), all data had a high correlation with the observed data (>0.97). The only exception was RRTMG(F)—0.85. The lowest values of correlation coefficient were found for days with a cold front—in the case of the WRF model: from 0.33 to 0.43; for ERA5 data: 0.76. The above comparison shows the superiority of the WRF data (with the RRTMG scheme applied) with respect to the ERA5 reanalyses in situations involving a cold front—0.72 and 0.65 versus 0.41, respectively. This is particularly evident on 26 August 2020.

Table 7. Error values: RMSE, nRMSE, MAE, MBE, nMBE for individual synoptic situations (ERA5).

Synoptic Situation	RMSE ($W \cdot m^{-2}$)	nRMSE (%)	MAE ($W \cdot m^{-2}$)	MBE ($W \cdot m^{-2}$)	nMBE (%)
High-pressure situation	54.37	29%	30.07	−23.60	−12.72%
Warm front	72.23	118%	36.03	12.44	20.41%
Cold front	88.02	128%	51.87	22.59	32.91%
Occluded front	146.58	837%	74.99	67.57	385.71%

Table 8. Error values: RMSE, nRMSE, MAE, MBE, nMBE for individual synoptic situations (RRTMG).

Synoptic Situation	RMSE ($W \cdot m^{-2}$)	nRMSE (%)	MAE ($W \cdot m^{-2}$)	MBE ($W \cdot m^{-2}$)	nMBE (%)
High-pressure situation	86.83	47%	54.62	−54.05	−29.14%
Warm front	178.98	294%	77.31	68.36	112.17%
Cold front	176.43	257%	94.80	29.69	43.24%
Occluded front	43.60	249%	16.51	3.30	19.01%

Table 9. Error values: RMSE, nRMSE, MAE, MBE, nMBE for individual synoptic situations (RRTMG(F)).

Synoptic Situation	RMSE ($W \cdot m^{-2}$)	nRMSE (%)	MAE ($W \cdot m^{-2}$)	MBE ($W \cdot m^{-2}$)	nMBE (%)
High-pressure situation	122.93	66%	60.24	−3.20	−1.72%
Warm front	228.32	375%	103.58	97.65	160.25%
Cold front	214.32	312%	113.51	37.86	55.14%
Occluded front	64.11	366%	25.20	13.05	74.50%

Table 10. Error values: RMSE, nRMSE, MAE, MBE, nMBE for individual synoptic situations (Dudhia).

Synoptic Situation	RMSE ($W \cdot m^{-2}$)	nRMSE (%)	MAE ($W \cdot m^{-2}$)	MBE ($W \cdot m^{-2}$)	nMBE (%)
High-pressure situation	38.79	21%	19.51	−3.61	−1.95%
Warm front	201.59	331%	98.98	93.87	154.04%
Cold front	195.02	284%	115.16	77.71	113.17%
Occluded front	51.92	296%	17.78	3.36	19.20%

Table 11. Pearson's correlation coefficients for individual synoptic situations.

Synoptic Situation	RRTMG	RRTMG(F)	Dudhia	ERA5
High-pressure situation	0.97	0.85	0.98	0.98
Warm front	0.57	0.54	0.61	0.87
Cold front	0.36	0.33	0.43	0.78
Occluded front	0.72	0.65	0.29	0.22
Mean value	**0.65**	**0.59**	**0.58**	**0.71**

The analysis of correlation coefficients for individual stations (Table 12) shows the dependence of forecast quality on geographical location. The highest correlation coefficients were obtained for the station located on Rügen Island (in the Baltic Sea)—Arkona

(>0.71). The lowest values of the correlation coefficient were obtained for the inland station Seehausen (0.56 to 0.81). The data that were closest to the measured data were those in the ERA5 reanalyses (mean 0.88), followed by Dudhia (0.72). Both RRTMG models obtained the same mean factor value of 0.64.

Table 12. Pearson's correlation coefficients for individual stations.

Station	RRTMG	RRTMG(F)	Dudhia	ERA5
Arkona	0.76	0.71	0.79	0.88
Rostock-Warnemünde	0.59	0.61	0.76	0.79
Seehausen	0.56	0.59	0.61	0.72
Mean value	**0.64**	**0.64**	**0.72**	**0.80**

From the point of view of users of renewable energy sources who are using solar radiation resources, an important aspect (one of the most important) is the daily sum reaching the device (photovoltaic panel, solar collector). Therefore, we also analyzed this parameter. The following tables (Tables 13–15) show the daily sums of direct radiation at each station obtained from the WRF model simulations, the ERA5 reanalyses, and the DWD station data.

A detailed analysis of daily sums shows that, depending on the synoptic situation, different WRF configurations perform better. Dudhia performed best (as expected) in high-pressure situations. RRTMG and RRTMG(F) worked very well for radiation forecasting during occluded fronts. The results were shown to be better than those obtained from the ERA5 reanalyses. For warm and cold fronts, the forecast from the RRTMG and RRTMG(F) model mostly overestimated the radiation values. However, it did not do so as much as Dudhia, for which the forecast values appear to be complete outliers. Considering the above, the advantage of the RRTMG model over the Dudhia model is noticeable when comparing the daily radiation sums.

Table 13. Summary of daily values of direct radiation at Arkona station [$W \cdot m^{-2}$].

Data	RRTMG	RRTMG(F)	Dudhia	DWD	ERA5
24022020 (WF)	1466.18	847.99	2108.85	519.44	649.97
14032020 (HPS)	1496.27	0.29	3301.72	3552.78	2885.94
11052020 (CF)	1985.60	1902.44	2862.07	1422.22	1501.67
22052020 (WF)	4521.05	5586.32	5348.84	3541.67	3498.88
28062020 (CF)	2518.94	2966.45	3613.35	1452.78	2382.94
26082020 (OF)	189.81	246.44	22.01	102.78	274.21
14092020 (HPS)	2769.83	4290.85	3605.88	3427.78	3366.34
06102020 (OF)	1286.10	1886.60	1256.94	983.33	2796.83

HPS—high-pressure situation; WF—warm front; CF—cold front; OF—occluded front.

Table 14. Summary of daily values of direct radiation at Rostock-Warnemünde station [W·m^{-2}].

Data	RRTMG	RRTMG(F)	Dudhia	DWD	ERA5
24022020 (WF)	557.83	552.89	421.13	180.56	227.38
14032020 (HPS)	2474.33	3850.48	3436.19	3630.56	2900.63
11052020 (CF)	475.64	62.44	1492.58	2355.56	2357.66
22052020 (WF)	3877.19	5128.08	5201.09	2377.78	2447.81
28062020 (CF)	3955.24	5204.99	2591.28	1200.00	1678.06
26082020 (OF)	88.08	172.97	72.80	25.00	94.65
14092020 (HPS)	2768.21	4170.89	3071.52	3491.67	3410.99
06102020 (OF)	335.26	459.00	177.14	411.11	2796.83

HPS—high-pressure situation; WF—warm front; CF—cold front; OF—occluded front.

Table 15. Summary of daily values of direct radiation at Seehausen station [W·m^{-2}].

Data	RRTMG	RRTMG(F)	Dudhia	DWD	ERA5
24022020 (WF)	119.75	256.23	198.79	16.67	69.31
14032020 (HPS)	2595.91	3989.22	3553.29	3411.11	2473.49
11052020 (CF)	753.31	195.63	2580.64	519.44	589.77
22052020 (WF)	4197.84	5708.39	4369.90	311.11	1472.05
28062020 (CF)	1523.99	1812.32	3546.85	877.78	1893.45
26082020 (OF)	94.79	241.40	121.64	30.56	127.83
14092020 (HPS)	2875.29	4475.20	3761.66	3627.78	3413.39
06102020 (OF)	382.77	478.59	730.16	444.44	2644.67

HPS—high-pressure situation; WF—warm front; CF—cold front; OF—occluded front.

5. Conclusions

The analyses described in this paper focused on the values of direct radiation reaching a flat surface, which enables further calculations of the received energy, taking into account factors such as the horizontal orientation of the panels, their tilt, and the use of tracking systems, etc. The maximum value of energy received in this way can be achieved through the optimal positioning of the panel plane in relation to the incident sunlight (at right angles) during its exposure to sunlight. To achieve this, it is necessary to use tracking systems that change the tilt of the panel in two planes depending on the current position of the sun.

The analyses performed demonstrate the possibility of forecasting the amount of direct radiation reaching the Earth's surface using the WRF numerical weather prediction model. Simulations were performed for two different shortwave radiation patterns (RRTMG and Dudhia); then, the obtained results were compared with data measured at actinometric stations for three points (DWD stations). In addition, the obtained data were compared with ERA5 reanalysis data. Of the WRF models tested, the one with the RRTMG scheme was found to be the most favorable (9% worse than the ERA5 data). The analysis of the results also highlighted the location for which the forecasts modeled by the WRF were characterized by the highest Pearson's correlation coefficient values—Arkona, located in the north of the region. The worst site in this respect was the inland station at Seehausen. At the same time, the forecast of direct radiation provides information on cloud cover (its characteristics, such as persistence time, compactness of cloud cover, etc.), which in turn make it possible to determine the presence of an atmospheric front (moving over the area during the forecast). In particular, the daily pattern of incoming direct radiation exhibits a decrease in amount (sometimes to a complete blackout), followed by an increase. Previous research on frontal detection showed better results for cold fronts than for warm

fronts. Among the synoptic situations analyzed in this paper, the most difficult to forecast were days with cold fronts, followed by those with warm fronts. Much better results were obtained for occluded fronts. The analyses also showed that the WRF model was able to correctly forecast the conditions associated with the occluded front, and did so significantly better than the ERA5 data (by 31%).

Due to the small number of studies addressing the analysis of the study region in terms of forecasting solar radiation, this study may serve to initiate research that will make it possible to find the optimal parameterization of the WRF model. In this way, the area will be better understood, enabling better adaptation of numerical forecasts for Central and Eastern Europe. High values of cloudiness still present a significant problem when forecasting many meteorological elements, especially those related to solar radiation. A closer understanding of conditions over the analyzed area will significantly improve the possibility of performing more effective forecasts.

Further planned research on the parameterization of the WRF model and local data assimilation, especially in the case of results obtained by ERA5, should allow for better results to be obtained in the future. The described analyses showed that RRTMG allows for better results than the Dudhia scheme. The presented results for model validation on the example of air temperature values showed a high level of convergence of the forecast data with the direct measurements; hence, further work should be focused on other parameters of the WRF physics model in order to achieve even better results.

Author Contributions: Conceptualization, M.M.; Formal analysis, M.M.; Investigation, M.M.; Methodology, M.M.; Supervision, K.K.; Validation, K.K. and A.A.; Visualization, A.A.; Writing—original draft, M.M. and A.A.; Writing—review and editing, M.M., K.K. and A.A. All authors have read and agreed to the published version of the manuscript.

Funding: This research and APC was funded by the Military University of Technology in Warsaw, Faculty of Civil Engineering and Geodesy, Institute of Geospatial Engineering and Geodesy statutory research funds UGB/22-785/2022/WAT.

Informed Consent Statement: Not applicable.

Data Availability Statement: Not applicable.

Acknowledgments: The authors send their special thanks to Wojciech Trześniak for assistance and consultation in preparing the synoptic description of this article. The authors acknowledge the DWD Climate Data Center (CDC) for providing the hourly station observation of solar incoming (total/diffuse) and longwave downward radiation for Germany. The authors acknowledge the Polish Institute of Meteorology and Water Management–National Research Institute (https://danepubliczne.imgw.pl/datastore) (accessed on 17 August 2021) for providing synoptic maps. Numerical simulations were performed using Weather Research Forecast version 4.2.1 (https://github.com/wrf-model/WRF/releases) (accessed on 21 August 2021). Maps were drawn using Generic Mapping Tools, version 6.1.1 (https://www.generic-mapping-tools.org/) (accessed on 1 January 2021).

Conflicts of Interest: The authors declare no conflict of interest.

References

1. Cross, S.; Hast, A.; Kuhi-Thalfeldt, R.; Syri, S.; Streimikiene, D.; Denina, A. Progress in renewable electricity in Northern Europe towards EU 2020 targets. *Renew. Sustain. Energy Rev.* **2015**, *52*, 1768–1780. [CrossRef]
2. Perpiña Castillo, C.; Batista e Silva, F.; Lavalle, C. An assessment of the regional potential for solar power generation in EU-28. *Energy Policy* **2016**, *88*, 86–99. [CrossRef]
3. Kim, J.Y.; Yun, C.Y.; Kim, C.K.; Kang, Y.H.; Kim, H.G.; Lee, S.N.; Kim, S.Y. Evaluation of WRF model-derived direct irradiance for solar thermal resource assessment over South Korea. *AIP Conf. Proc.* **2017**, *1850*, 140013. [CrossRef]
4. Azad, E. Assessment of three types of heat pipe solar collectors. *Renew. Sustain. Energy Rev.* **2012**, *16*, 2833–2838. [CrossRef]
5. Sabiha, M.A.; Saidur, R.; Mekhilef, S.; Mahian, O. Progress and latest developments of evacuated tube solar collectors. *Renew. Sustain. Energy Rev.* **2015**, *51*, 1038–1054. [CrossRef]
6. Sarmiento, N.; Belmonte, S.; Dellicompagni, P.; Franco, J.; Escalante, K.; Sarmiento, J. A solar irradiation GIS as decision support tool for the Province of Salta, Argentina. *Renew. Energy* **2019**, *132*, 68–80. [CrossRef]

7. Abu Taha, R.; Daim, T. Multi-Criteria Applications in Renewable Energy Analysis, a Literature Review. *Green Energy Technol.* **2013**, *60*, 17–30. [CrossRef]
8. Mierzwiak, M.; Calka, B. Multi-Criteria Analysis for Solar Farm Location Suitability. *Rep. Geod. Geoinf.* **2017**, *104*, 20–32. [CrossRef]
9. Mokarram, M.; Mokarram, M.J.; Khosravi, M.R.; Saber, A.; Rahideh, A. Determination of the optimal location for constructing solar photovoltaic farms based on multi-criteria decision system and Dempster–Shafer theory. *Sci. Rep.* **2020**, *10*, 8200. [CrossRef]
10. Rich, P.M.; Hetrick, W.A.; Saving, S.C. *Modeling Topographic Influences on Solar Radiation: A Manual for the SOLARFLUX Model*; Los Alamos National Lab. (LANL): Los Alamos, NM, USA, 1995. [CrossRef]
11. Fu, P.; Rich, P.M. A geometric solar radiation model and its applications in agriculture and forestry. In Proceedings of the Second International Conference on Geospatial Information in Agriculture and Forestry, Lake Buena Vista, FL, USA, 10–12 January 2000; pp. 357–364.
12. Tovar-Pescador, J.; Pozo-Vázquez, D.; Ruiz-Arias, J.A.; Batlles, J.; López, G.; Bosch, J.L. On the use of the digital elevation model to estimate the solar radiation in areas of complex topography. *Meteorol. Appl.* **2006**, *13*, 279–287. [CrossRef]
13. Ramirez-Vergara, J.; Bosman, L.B.; Leon-Salas, W.D.; Wollega, E. Ambient temperature and solar irradiance forecasting prediction horizon sensitivity analysis. *Mach. Learn. Appl.* **2021**, *6*, 100128. [CrossRef]
14. Yang, F.; Pan, H.L.; Krueger, S.K.; Moorthi, S.; Lord, S.J. Evaluation of the NCEP Global Forecast System at the ARM SGP Site. *Mon. Weather Rev.* **2006**, *134*, 3668–3690. [CrossRef]
15. Brown, A.; Milton, S.; Cullen, M.; Golding, B.; Mitchell, J.; Shelly, A. Unified Modeling and Prediction of Weather and Climate: A 25-Year Journey. *Bull. Am. Meteorol. Soc.* **2012**, *93*, 1865–1877. [CrossRef]
16. Describing ECMWF's Forecasts and Forecasting System. ECMWF. Available online: https://www.ecmwf.int/en/elibrary/17412-describing-ecmwfs-forecasts-and-forecasting-system (accessed on 16 March 2022).
17. Zängl, G.; Reinert, D.; Rípodas, P.; Baldauf, M. The ICON (ICOsahedral Non-hydrostatic) modeling framework of DWD and MPI-M: Description of the non-hydrostatic dynamical core. *Q. J. R. Meteorol. Soc.* **2015**, *141*, 563–579. [CrossRef]
18. Powers, J.G.; Klemp, J.B.; Skamarock, W.C.; Davis, C.A.; Dudhia, J.; Gill, D.O.; Coen, J.L.; Gochis, D.J.; Ahmadov, R.; Peckham, S.E.; et al. The Weather Research and Forecasting Model: Overview, System Efforts, and Future Directions. *Bull. Am. Meteorol. Soc.* **2017**, *98*, 1717–1737. [CrossRef]
19. Weather Research and Forecasting Model. MMM: Mesoscale & Microscale Meteorology Laboratory. Available online: https://www.mmm.ucar.edu/weather-research-and-forecasting-model (accessed on 16 March 2022).
20. Mandal, A.; Nykiel, G.; Strzyzewski, T.; Kochanski, A.; Wrońska, W.; Gruszczynska, M.; Figurski, M.; Mandal, A.; Nykiel, G.; Strzyzewski, T.; et al. High-resolution fire danger forecast for Poland based on the Weather Research and Forecasting Model. *Int. J. Wildl. Fire* **2021**, *31*, 149–162. [CrossRef]
21. Nilo, S.T.; Cimini, D.; Di Paola, F.; Gallucci, D.; Gentile, S.; Geraldi, E.; Larosa, S.; Ricciardelli, E.; Ripepi, E.; Viggiano, M.; et al. Fog Forecast Using WRF Model Output for Solar Energy Applications. *Energies* **2020**, *13*, 6140. [CrossRef]
22. Guo, Z.; Xiao, X. Wind power assessment based on a WRF wind simulation with developed power curve modeling methods. *Abstr. Appl. Anal.* **2014**, *2014*, 941648. [CrossRef]
23. Tan, E.; Mentes, S.S.; Unal, E.; Unal, Y.; Efe, B.; Barutcu, B.; Onol, B.; Topcu, H.S.; Incecik, S. Short term wind energy resource prediction using WRF model for a location in western part of Turkey. *J. Renew. Sustain. Energy* **2021**, *13*, 013303. [CrossRef]
24. Jimenez, P.A.; Hacker, J.P.; Dudhia, J.; Haupt, S.E.; Ruiz-Arias, J.A.; Gueymard, C.A.; Thompson, G.; Eidhammer, T.; Deng, A. WRF-SOLAR: Description and clear-sky assessment of an augmented NWP model for solar power prediction. *Bull. Am. Meteorol. Soc.* **2016**, *97*, 1249–1264. [CrossRef]
25. Jiménez, P.A.; Alessandrini, S.; Haupt, S.E.; Deng, A.; Kosovic, B.; Lee, J.A.; Monache, L.D. The role of unresolved clouds on short-range global horizontal irradiance predictability. *Mon. Weather Rev.* **2016**, *144*, 3099–3107. [CrossRef]
26. Lee, J.A.; Haupt, S.E.; Jiménez, P.A.; Rogers, M.A.; Miller, S.D.; McCandless, T.C. Solar irradiance nowcasting case studies near sacramento. *J. Appl. Meteorol. Climatol.* **2017**, *56*, 85–108. [CrossRef]
27. Ruiz-Arias, J.A.; Dudhia, J. A simple parameterization of the short-wave aerosol optical properties for surface direct and diffuse irradiances assessment in a numerical weather model. *Geosci. Model Dev.* **2014**, *7*, 593–629. [CrossRef]
28. Gueymard, C.; Jimenez, P. Validation of Real-Time Solar Irradiance Simulations Over Kuwait Using WRF-Solar. In Proceedings of the EuroSun 2018 Conference, Rapperswil, Switzerland, 10–13 September 2018; pp. 1–11. [CrossRef]
29. Diagne, M.; David, M.; Boland, J.; Schmutz, N.; Lauret, P. ScienceDirect 2013 ISES Solar World Congress Post-processing of solar irradiance forecasts from WRF Model at Reunion Island Selection and/or peer-review under responsibility of ISES. *Energy Procedia* **2014**, *57*, 1364–1373. [CrossRef]
30. Zempila, M.-M.; Giannaros, T.M.; Bais, A.; Melas, D.; Kazantzidis, A. Evaluation of WRF shortwave radiation parameterizations in predicting Global Horizontal Irradiance in Greece. *Renew. Energy* **2016**, *86*, 831–840. [CrossRef]
31. Lara-Fanego, V.; Ruiz-Arias, J.A.; Pozo-Vázquez, D.; Santos-Alamillos, F.J.; Tovar-Pescador, J. Evaluation of the WRF model solar irradiance forecasts in Andalusia (southern Spain). *Sol. Energy* **2012**, *86*, 2200–2217. [CrossRef]
32. Isvoranu, D.; Badescu, V. Comparison Between Measurements and WRF Numerical Simulation of Global Solar Irradiation in Romania. *Ann. West Univ. Timis.-Phys.* **2013**, *57*, 24–33. [CrossRef]
33. Incecik, S.; Sakarya, S.; Tilev, S.; Kahraman, A.; Aksoy, B.; Caliskan, E.; Topcu, S.; Kahya, C.; Odman, M.T. Evaluation of WRF parameterizations for global horizontal irradiation forecasts: A study for Turkey. *Atmosfera* **2019**, *32*, 143–158. [CrossRef]

34. Perez, R.; Lorenz, E.; Pelland, S.; Beauharnois, M.; Van Knowe, G.; Hemker, K.; Heinemann, D.; Remund, J.; Müller, S.C.; Traunmüller, W.; et al. Comparison of numerical weather prediction solar irradiance forecasts in the US, Canada and Europe. *Sol. Energy* **2013**, *94*, 305–326. [CrossRef]
35. Kallio-Myers, V.; Riihelä, A.; Schoenach, D.; Gregow, E.; Carlund, T.; Lindfors, A.V. Comparison of irradiance forecasts from operational NWP model and satellite-based estimates over Fennoscandia. *Meteorol. Appl.* **2022**, *29*, e2051. [CrossRef]
36. Beck, H.E.; Zimmermann, N.E.; McVicar, T.R.; Vergopolan, N.; Berg, A.; Wood, E.F. Present and future Köppen-Geiger climate classification maps at 1-km resolution. *Sci. Data* **2018**, *5*, 180214. [CrossRef]
37. Schemm, S.; Sprenger, M.; Martius, O.; Wernli, H.; Zimmer, M.; Schemm, S.; Sprenger, M.; Martius, O.; Wernli, H.; Zimmer, M. Increase in the number of extremely strong fronts over Europe? A study based on ERA-Interim reanalysis (1979–2014). *GeoRL* **2017**, *44*, 553–561. [CrossRef]
38. Catto, J.L.; Ackerley, D.; Booth, J.F.; Champion, A.J.; Colle, B.A.; Pfahl, S.; Pinto, J.G.; Quinting, J.F.; Seiler, C. The Future of Midlatitude Cyclones. *Curr. Clim. Chang. Rep.* **2019**, *5*, 407–420. [CrossRef]
39. Catto, J.L.; Nicholls, N.; Jakob, C.; Shelton, K.L. Atmospheric fronts in current and future climates. *Geophys. Res. Lett* **2014**, *41*, 7642–7650. [CrossRef]
40. Raible, C.C. On the relation between extremes of midlatitude cyclones and the atmospheric circulation using ERA40. *Geophys. Res. Lett.* **2007**, *34*, L07703. [CrossRef]
41. IPCC. Summary for Policymakers. In *Climate Change 2021: The Physical Science Basis. Contribution of Working Group I to the Sixth Assessment Report of the Intergovernmental Panel on Climate Change*; Masson-Delmotte, V., Zhai, P., Pirani, A., Connors, S.L., Péan, C., Berger, S., Caud, N., Chen, Y., Goldfarb, L., Gomis, M.I., et al., Eds.; Cambridge University Press: Cambridge, UK, 2021.
42. Bochenek, B.; Ustrnul, Z.; Wypych, A.; Kubacka, D. Machine Learning-Based Front Detection in Central Europe. *Atmos* **2021**, *12*, 1312. [CrossRef]
43. Sykulski, P.; Bielec-Bąkowska, Z. Atmospheric fronts over Poland (2006–2015). *Environ. Socio-Econ. Stud.* **2017**, *5*, 29–39. [CrossRef]
44. Hersbach, H.; Bell, B.; Berrisford, P.; Hirahara, S.; Horányi, A.; Muñoz-Sabater, J.; Nicolas, J.; Peubey, C.; Radu, R.; Schepers, D.; et al. The ERA5 global reanalysis. *Q. J. R. Meteorol. Soc.* **2020**, *146*, 1999–2049. [CrossRef]
45. Radiation Quantities in the ECMWF Model and MARS. Available online: https://www.ecmwf.int/en/elibrary/18490-radiation-quantities-ecmwf-model-and-mars (accessed on 21 August 2021).
46. DWD Climate Data Center (CDC): Hourly Station Observations of Solar Incoming (Total/Diffuse) and Longwave downward Radiation for Germany, Version Recent. Available online: https://opendata.dwd.de/climate_environment/CDC/observations_germany/climate/hourly/solar/DESCRIPTION_obsgermany_climate_hourly_solar_en.pdf (accessed on 21 August 2021).
47. De Araujo, J.M.S. Performance comparison of solar radiation forecasting between wrf and lstm in Gifu, Japan. *Environ. Res. Commun.* **2020**, *2*, 045002. [CrossRef]
48. Chai, T.; Draxler, R.R. Root mean square error (RMSE) or mean absolute error (MAE)?-Arguments against avoiding RMSE in the literature. *Geosci. Model Dev.* **2014**, *7*, 1247–1250. [CrossRef]
49. Willmott, C.J.; Matsuura, K. Advantages of the mean absolute error (MAE) over the root mean square error (RMSE) in assessing average model performance. *Clim. Res.* **2005**, *30*, 79–82. [CrossRef]
50. Jerzy Kondracki Fizycznogeograficzna regionalizacja Niemiec i terenów przyległych w układzie dzisiętnym. *Przegląd Geogr.* **1997**, *69*, 141–148.
51. IMGW Public Data. Available online: https://danepubliczne.imgw.pl/datastore (accessed on 15 March 2022).
52. National Centers for Environmental Prediction/National Weather Service/NOAA/U.S. Department of Commerce. 2015, Updated Daily. NCEP GFS 0.25 De-gree Global Forecast Grids Historical Archive. Research Data Archive at the National Center for Atmospheric Res. Available online: https://rda.ucar.edu/datasets/ds084.1/ (accessed on 21 August 2021).
53. Skamarock, W.C.; Klemp, J.B. A time-split nonhydrostatic atmospheric model for weather research and forecasting applications. *J. Comput. Phys.* **2008**, *227*, 3465–3485. [CrossRef]
54. Thompson, G.; Tewari, M.; Ikeda, K.; Tessendorf, S.; Weeks, C.; Otkin, J.; Kong, F. Explicitly-coupled cloud physics and radiation parameterizations and subsequent evaluation in WRF high-resolution convective forecasts. *Atmos. Res.* **2016**, *168*, 92–104. [CrossRef]
55. Dudhia, J. Numerical Study of Convection Observed during the Winter Monsoon Experiment Using a Mesoscale Two-Dimensional Model. *J. Atmos. Sci.* **1989**, *46*, 3077–3107. [CrossRef]
56. Xie, Y.; Sengupta, M.; Dudhia, J. A Fast All-sky Radiation Model for Solar applications (FARMS): Algorithm and performance evaluation. *Sol. Energy* **2016**, *135*, 435–445. [CrossRef]
57. Cohan, D.S.; Xu, J.; Greenwald, R.; Bergin, M.H.; Chameides, W.L. Impact of atmospheric aerosol light scattering and absorption on terrestrial net primary productivity. *Glob. Biogeochem. Cycles* **2002**, *16*, 37-1–37-12. [CrossRef]
58. Documentacion. Available online: https://www.ogimet.com/guia.phtml.en (accessed on 15 March 2022).